Tetrahedral shape of ^{110}Zr from covariant density functional theory in 3D lattice space

F. F. Xu (许方方) [1], B. Li (李博) [1], Z. X. Ren (任政学) [1,2,3] and P. W. Zhao (赵鹏巍) [1,*]

[1]*State Key Laboratory of Nuclear Physics and Technology, School of Physics, Peking University, Beijing 100871, China*
[2]*Institut für Kernphysik, Institute for Advanced Simulation and Jülich Center*
for Hadron Physics, Forschungszentrum Jülich, D-52425 Jülich, Germany
[3]*Helmholtz-Institut für Strahlen- und Kernphysik and Bethe Center*
for Theoretical Physics, Universität Bonn, D-53115 Bonn, Germany

Covariant density functional theory is solved in 3D lattice space by implementing the preconditioned conjugate gradient method with a filtering function. It considerably improves the computational efficiency compared to the previous inverse Hamiltonian method (IHM). This new method is then applied to explore the tetrahedral shape of ^{110}Zr in the full deformation space. Although the ground-state energy and deformation are consistent with the previous study, the pear-shaped isomeric state is significantly lowered in energy. The energy difference between the two states is only 0.07 MeV, indicating an interesting possible shape coexistence in ^{110}Zr. This effect is analyzed with the microscopic evolution of the single-particle levels near the Fermi surface driven by the deformation.

I. INTRODUCTION

The occurrence of spontaneous symmetry breaking leads to shapes with a variety of symmetries for nuclei. Nuclear shape can be described by the parametrization of the nuclear surface with a multipole expansion of spherical harmonics $Y_{\lambda\mu}$ [1]. The quadrupole shape with axial symmetry characterized by the Y_{20}-type deformation has been known for a long time, which results in rotational excitation in nuclei [1]. In recent decades, many efforts have been devoted to studying the triaxiality [2–5] and reflection asymmetry [6–9] in nuclei, characterized by the Y_{22}- and the Y_{30}-type deformations, respectively. Novel excitation modes have been predicted theoretically to identify these shapes in nuclei [1,2,10,11], and many of them have been confirmed experimentally [3,4]. Indeed, exotic shapes that violate both reflection and axial symmetries, such as tetrahedral shapes, may also exist in nuclei.

A tetrahedral shape corresponds to a pure Y_{32}-type deformation. The tetrahedral symmetry of nuclei is a direct consequence of the point group T_d^D, which has two two-dimensional and one four-dimensional irreducible representations [12]. Due to the tetrahedral symmetry, the single-particle levels split into multiplets with degeneracies equal to the irreducible representations of the T_d^D group. A fourfold degeneracy results in large energy gaps in the single-particle spectrum, and these gaps are comparable to or even larger than the well-known spherical shell gaps. Empirically, these large gaps occur predominantly in nuclei with $Z(N) =$ 16, 20, 32, 40, 56, 70, and 90, and $N =$ 112, 136, and 142 [13–18]. Thus, a nucleus with proton and/or neutron numbers

equal to these values may have a static tetrahedral deformation, characterized by the occurrence of negative-parity bands with missing in-band $E2$ transitions [19,20].

Several experiments have been devoted to identifying the tetrahedral shape of nuclei. The negative-parity bands in ^{160}Yb and ^{154,156}Gd have been suggested as candidates for the rotational bands of tetrahedral nuclei [21], but the measured nonzero quadrupole moments contradict the existence of tetrahedral shapes in these nuclei [19,20,22]. For other candidates in nuclei ^{230,232}U [23], the possibilities of tetrahedral shapes for the negative-parity bands in ^{230,232}U appear difficult to reconcile with the systematics of measured quadrupole moments for the neighboring isotone ^{226}Ra [24]. The isomeric state of ^{108}Zr is proposed to be a candidate for a tetrahedral shape isomer [25], while the measurement of the corresponding band structure is required to confirm the tetrahedral shape. The ^{156}Dy has been suggested as a tetrahedral candidate nucleus [26], but it is not supported from the experimental $B(E2)/B(E1)$ ratios of transition probabilities for the negative-parity bands [27]. In conclusion, there is still no firm experimental evidence to support the existence of tetrahedral shapes in nuclei.

The possible tetrahedral shapes in the ground or isomeric states of nuclei have been investigated with many theoretical approaches. For example, the macroscopic-microscopic (MM) model [14,15,21,28–31], the algebraic cluster model [32], the reflection asymmetric shell model [33,34], the nonrelativistic density functional theories (DFTs) [28,35–42], and the covariant density functional theories (CDFTs) [43,44]. The CDFT [45] is of particular interest, since it brings many advantages to describe the nuclear systems [46–48], such as the natural inclusion of the self-consistent treatment of the time-odd fields [49] and spin-orbit interactions, which can be

*pwzhao@pku.edu.cn

clearly seen in the nonrelativistic reduction of the CDFT via a similarity renormalization method [50]. However, up to now, the V_4 symmetry has always been assumed in the application of CDFT to nuclear tetrahedral shapes [43,44].

The aim of the present work is to explore the tetrahedral shapes of nuclei in the full deformation space by solving the CDFT in three-dimensional (3D) lattice space. The CDFT in 3D lattice space has been a longstanding challenge due to the variational collapse [51] and the Fermion doubling [52] problems. It became available recently [53] with the help of the inverse Hamiltonian method (IHM) [54] and the Fourier spectral method [55]. In Ref. [56], a more efficient method, the preconditioned conjugate gradient method with a filtering function (PCG-F), is proposed to solve the nuclear Dirac equation with a given potential in 3D lattice space. In this work, the CDFT will be solved in 3D lattice space by implementing the PCG-F method [56], and this new method is then applied to explore the tetrahedral shape of ^{110}Zr in the full deformation space. Note that the ground state of ^{110}Zr was previously predicted to be tetrahedral by the MM model [28], the Skyrme DFTs [28,37], and the multidimensionally constrained CDFT (MDC-CDFT) [43].

The paper is organized as follows. The formulas for the CDFT and the PCG-F method will be briefly introduced in Sec. II. The numerical details are presented in Sec. III. Section IV is devoted to the results for tetrahedral shapes in ^{110}Zr. A summary is given in Sec. V.

II. THEORETICAL FRAMEWORK

A. Formalism of the CDFT

The starting point of the CDFT is a standard Lagrangian density in the point-coupling form, which can be written as [57]

$$
\begin{aligned}
\mathcal{L} = \ &\bar{\psi}(i\gamma^\mu \partial_\mu - m)\psi - \frac{1}{2}\alpha_S(\bar{\psi}\psi)(\bar{\psi}\psi) \\
&- \frac{1}{2}\alpha_V(\bar{\psi}\gamma^\mu\psi)(\bar{\psi}\gamma_\mu\psi) - \frac{1}{2}\alpha_{TV}(\bar{\psi}\vec{\tau}\gamma^\mu\psi) \\
&\cdot(\bar{\psi}\vec{\tau}\gamma_\mu\psi) - \frac{1}{3}\beta_S(\bar{\psi}\psi)^3 - \frac{1}{4}\gamma_S(\bar{\psi}\psi)^4 \\
&- \frac{1}{4}\gamma_V[(\bar{\psi}\gamma^\mu\psi)(\bar{\psi}\gamma_\mu\psi)]^2 - \frac{1}{2}\delta_S\partial^\nu(\bar{\psi}\psi)\partial_\nu(\bar{\psi}\psi) \\
&- \frac{1}{2}\delta_V\partial^\nu(\bar{\psi}\gamma^\mu\psi)\partial_\nu(\bar{\psi}\gamma_\mu\psi) - \frac{1}{2}\delta_{TV}\partial^\nu(\bar{\psi}\vec{\tau}\gamma^\mu\psi) \\
&\cdot\partial_\nu(\bar{\psi}\vec{\tau}\gamma_\mu\psi) - \frac{1}{4}F^{\mu\nu}F_{\mu\nu} - e\frac{1-\tau_3}{2}(\bar{\psi}\gamma^\mu\psi)A_\mu, \quad (1)
\end{aligned}
$$

where m is the nucleon mass. According to the conventional variational principle, one obtains the Dirac equation for nucleons,

$$
\begin{aligned}
\hat{h}(\boldsymbol{r})\psi_k(\boldsymbol{r}) &= [\boldsymbol{\alpha}\cdot(-i\boldsymbol{\nabla} - \boldsymbol{V}(\boldsymbol{r})) + \beta(m + S(\boldsymbol{r})) + V^0(\boldsymbol{r})] \\
\psi_k(\boldsymbol{r}) &= \varepsilon_k\psi_k(\boldsymbol{r}), \quad (2)
\end{aligned}
$$

where ε_k is the single-particle energy. The single-particle Dirac Hamiltonian $\hat{h}(\boldsymbol{r})$ contains the scalar $S(\boldsymbol{r})$ and

four-vector $V^\mu(\boldsymbol{r})$ potentials,

$$
S(\boldsymbol{r}) = \alpha_S\rho_S + \beta_S\rho_S^2 + \gamma_S\rho_S^3 + \delta_S\Delta\rho_S, \quad (3a)
$$

$$
\begin{aligned}
V^\mu(\boldsymbol{r}) = \ &\alpha_V j^\mu + \gamma_V(j^\mu j_\mu)j^\mu + \delta_V\Delta j^\mu + \tau_3\alpha_{TV}j_{TV}^\mu \\
&+ \tau_3\delta_{TV}\Delta j_{TV}^\mu + e\frac{1-\tau_3}{2}A^\mu, \quad (3b)
\end{aligned}
$$

where the electromagnetic field A^μ is determined by Poisson's equation, and the densities and currents are defined as

$$
\rho_S(\boldsymbol{r}) = \sum_k v_k^2\bar{\psi}_k(\boldsymbol{r})\psi_k(\boldsymbol{r}), \quad (4a)
$$

$$
j^\mu(\boldsymbol{r}) = \sum_k v_k^2\bar{\psi}_k(\boldsymbol{r})\gamma^\mu\psi_k(\boldsymbol{r}), \quad (4b)
$$

$$
\vec{j}_{TV}^\mu(\boldsymbol{r}) = \sum_k v_k^2\bar{\psi}_k(\boldsymbol{r})\gamma^\mu\vec{\tau}_3\psi_k(\boldsymbol{r}), \quad (4c)
$$

$$
j_c^\mu(\boldsymbol{r}) = \sum_k v_k^2\bar{\psi}_k(\boldsymbol{r})\gamma^\mu\frac{1-\tau_3}{2}\psi_k(\boldsymbol{r}). \quad (4d)
$$

Here, τ_3 is the isospin Pauli matrix with the eigenvalues $+1$ for neutrons and -1 for protons. The time component of the vector current j^μ is usually denoted as the vector density ρ_v.

For open shell nuclei, pairing correlations play an important role, and they are taken into account with the Bardeen-Cooper-Schrieffer (BCS) method. The pairing energy functional is given by

$$
E_{\text{pair}} = -\sum_{\tau=n,p}\frac{G_\tau}{4}\int d^3r\kappa_\tau^*(\boldsymbol{r})\kappa_\tau(\boldsymbol{r}), \quad (5)
$$

where G_τ is the constant pairing strength and $\kappa(\boldsymbol{r})$ is the pairing tensor,

$$
\kappa(\boldsymbol{r}) = 2\sum_{k>0}f_k u_k v_k|\psi_k(\boldsymbol{r})|^2 \quad (6)
$$

with the smooth-cutoff weight factor

$$
f_k = \frac{\Theta(-\varepsilon_k)}{1 + \exp[(\varepsilon_k - \lambda_{\text{F}} - \Delta E_\tau)/\mu_\tau]}. \quad (7)
$$

Here, the Fermi energy λ_{F} is determined by the particle number, $2\sum_{k>0}v_k^2 = N_\tau$, with N_τ the particle number of neutrons or protons. The cutoff parameters $\Delta E_\tau = 5$ MeV and $\mu_\tau = \Delta E_\tau/10 = 0.5$ MeV are chosen as in Ref. [58]. $\Theta(-\varepsilon_k)$ equals one for bound levels and zero elsewhere, and it is introduced to exclude the continuum in the pairing window.

B. Implementation of the PCG-F method

In the PCG-F method, the lowest $\tilde{A}$ eigenstates in the Fermi sea of the Dirac equation (2) are solved iteratively starting from a set of orthonormalized guess solutions $\psi_k^{(0)}$ ($k = 1, 2, \ldots, \tilde{A}$). Here, the value of $\tilde{A}$ is chosen to include all bound states. The trial wave function ψ_k is then updated iteratively,

$$
\begin{aligned}
\psi_k^{(i+1)} &= \sum_{l=1}^{\tilde{A}}[G_{kl}^a X_l^{(i)} + G_{kl}^b W_l^{(i)} + G_{kl}^c P_l^{(i)}], \\
&(i = 0, 1, 2, \ldots), \quad (8)
\end{aligned}
$$

where $X_l^{(i)}$, $W_l^{(i)}$, and $P_l^{(i)}$ are defined as

$$X_l^{(i)} = F(\hat{h}^{(i)})\psi_l^{(i)}, \tag{9a}$$

$$W_l^{(i)} = F^4(\hat{h}^{(i)})T_l^{(i)}\big[\hat{h}^{(i)} - \langle\psi_l^{(i)}|\hat{h}^{(i)}|\psi_l^{(i)}\rangle\big]\psi_l^{(i)}, \tag{9b}$$

$$P_l^{(i)} = F(\hat{h}^{(i)})\left[\psi_l^{(i)} - \sum_{l'=1}^{\tilde{A}}\langle\psi_{l'}^{(i-1)}|\psi_l^{(i)}\rangle\psi_{l'}^{(i-1)}\right]. \tag{9c}$$

The initial $P_l^{(0)}$ is set to zero. The filtering operator $F(\hat{h})$ and the preconditioner T_l are introduced for the sake of iteration convergence. The single-particle Dirac Hamiltonian $\hat{h}^{(i)}$ is constructed from the densities and currents determined by the wave functions $\{\psi_k^{(i)}\}$. The coefficient matrices G^a, G^b, and G^c in Eq. (8) are chosen to minimize $\sum_{k=1}^{\tilde{A}}\langle\psi_k^{(i+1)}|\hat{h}^{(i)}|\psi_k^{(i+1)}\rangle$ under the orthonormalization condition $\langle\psi_k^{(i+1)}|\psi_l^{(i+1)}\rangle = \delta_{kl}$.

Similar to Ref. [56], the filtering operator $F(\hat{h})$ and the preconditioner T_l read

$$F(\hat{h}^{(i)}) = \big(\hat{h}^{(i)} + 2m\big)^2, \tag{10}$$

$$T_l^{(i)} = \big[\hat{p}^2 + (g_l^{(i)}m)^2\big]^{-1} \tag{11}$$

with

$$g_l^{(i)} = 0.15\frac{\langle\psi_l^{(i)}|\hat{h}^{(i)}|\psi_l^{(i)}\rangle}{(V^0 + S)_{\min}} + 0.10. \tag{12}$$

There are two criteria for the convergence of the iteration. One is that the energy dispersions $\langle\psi_l^{(i)}|[\hat{h}^{(i)}]^2|\psi_l^{(i)}\rangle - \langle\psi_l^{(i)}|\hat{h}^{(i)}|\psi_l^{(i)}\rangle^2$ for all occupied levels should be smaller than a certain value, e.g., 10^{-8} MeV^2. The other one is that the differences between the mean potentials [Eqs. (4a) and (4b)] at two adjacent iterations should be smaller than a certain value. The convergence is achieved only if both criteria are satisfied.

C. Nuclear bulk properties

From the converged wave functions, the nuclear total energy and the deformation parameters can be calculated. The total energy consists of the mean-field energy E_{MF}, the pairing energy E_{pair}, and the center-of-mass (c.m.) correction energy $E_{\mathrm{c.m.}}$:

$$E_{\mathrm{tot}} = E_{\mathrm{MF}} + E_{\mathrm{pair}} + E_{\mathrm{c.m.}}, \tag{13}$$

where the mean-field energy E_{MF} is written as

$$\begin{aligned}
E_{\mathrm{MF}} = \int d^3r\bigg\{ &\sum_k v_k^2\psi_k^\dagger(\boldsymbol{\alpha}\cdot\boldsymbol{p} + \beta m)\psi_k + \frac{\alpha_S}{2}\rho_S^2 + \frac{\alpha_V}{2}j^\mu j_\mu \\
&+ \frac{\alpha_{TV}}{2}\vec{j}_{TV}^\mu\cdot(\vec{j}_{TV})_\mu + \frac{\beta_S}{3}\rho_S^3 + \frac{\gamma_S}{4}\rho_S^4 + \frac{\gamma_V}{4}(j^\mu j_\mu)^2 \\
&+ \frac{\delta_S}{2}\rho_S\Delta\rho_S + \frac{\delta_V}{2}j^\mu\Delta j_\mu + \frac{\delta_{TV}}{2}\vec{j}_{TV}^\mu \\
&\cdot\Delta(\vec{j}_{TV})_\mu + \frac{1}{2}A_\mu\Delta A^\mu + ej_c^\mu A_\mu\bigg\}.
\end{aligned} \tag{14}$$

The pairing energy E_{pair} is calculated following Eq. (6), and the c.m. correction energy $E_{\mathrm{c.m.}}$ is considered with the
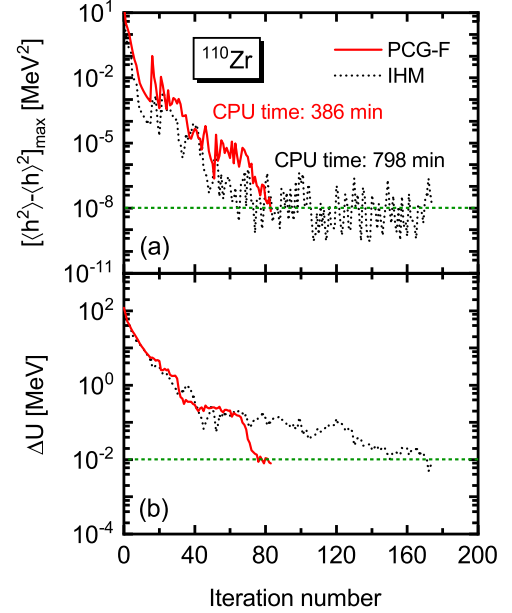

FIG. 1. The maximum energy dispersion for the occupied single-particle states (a), and the maximum absolute difference between the mean potentials (including the scalar and vector potentials) at two adjacent iterations (b), as functions of the iteration number for the ground state of ^{110}Zr. The solid and dotted curves, respectively, represent the results calculated by the PCG-F and IHM, and the corresponding computation times are also given.

microscopic c.m. correction

$$E_{\mathrm{c.m.}} = -\frac{1}{2mA}\langle\boldsymbol{P}_{\mathrm{c.m.}}^2\rangle \tag{15}$$

with A the mass number and $\boldsymbol{P}_{\mathrm{cm}} = \sum_k \boldsymbol{p}_k$ the total momentum in the c.m. frame.

For a quadrupole shape, the intrinsic frame can be defined by aligning the principal axes of inertia of the nucleus along the coordinate axes of the 3D box. The two quadrupole deformation parameters a_{20} and a_{22} are then obtained with

$$a_{20} = \frac{4\pi}{3AR^2}\cdot\int d^3r\rho_v(\boldsymbol{r})r^2Y_{20}, \tag{16a}$$

$$a_{22} = \frac{4\pi}{3AR^2}\cdot\int d^3r\rho_v(\boldsymbol{r})r^2Y_{22}, \tag{16b}$$

where $R = 1.2 \times A^{1/3}$ fm. For a general quadrupole-octupole shape, however, the principal axes for the quadrupole and octupole degrees of freedom are not the same, so a natural intrinsic frame related to the symmetry of the shape does not exist and many alternative ways can be used to define the intrinsic frame. Here, we keep the intrinsic frame as defined by the pure quadrupole deformation case, and two quadrupole deformation parameters and seven octupole deformation parameters are then used to describe the shape. The ground-state energy can be obtained by self-consistent calculations in such a high dimensional deformation space. By constraining the a_{20} deformation to certain values, a potential energy curve against the a_{20} deformation can also be obtained (see Fig. 2).

In the present work, we are interested in the ground state of ^{110}Zr, whose quadrupole deformation is indeed zero (see
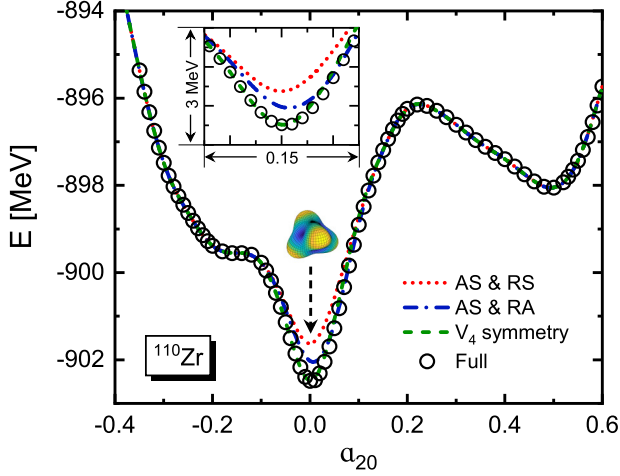
FIG. 2. The potential energy curves of ^{110}Zr calculated with the CDFT in 3D lattice space by imposing different symmetries. The results restricted to axial symmetry and reflection symmetry (AS & RS), axial symmetry and reflection asymmetry (AS & RA), and V_4 symmetry are represented by dotted, dashed-dotted, and dashed lines, respectively. The open circles represent the results without any symmetry restriction (Full), and the obtained ground-state shape is illustrated by the 3D image. The inset zooms in to the detailed structure of the potential energy curves near $a_{20} = 0$.

Fig. 2), i.e., a pure octuple shape. Consequently, the nuclear surface R can be parametrized as [59]

$$R = R_0 \left[1 + \epsilon_0 A_2 + \sum_{i=1}^{3} \epsilon_1(i) F_1(i) + \sum_{i=1}^{3} \epsilon_2(i) F_2(i) \right], \quad (17)$$

where A_2, $F_1(i)$, and $F_2(i)$ are related to the irreducible representations of the octahedron group,

$$A_2 = -\frac{i}{2}(Y_{32} - Y_{3-2}), \quad (18a)$$

$$F_1(1) = Y_{30}, \quad (18b)$$

$$F_1(2) = -\frac{\sqrt{5}}{4}(Y_{33} - Y_{3-3}) + \frac{\sqrt{3}}{4}(Y_{31} - Y_{3-1}), \quad (18c)$$

$$F_1(3) = -i\frac{\sqrt{5}}{4}(Y_{33} + Y_{3-3}) - i\frac{\sqrt{3}}{4}(Y_{31} + Y_{3-1}), \quad (18d)$$

$$F_2(1) = \frac{1}{\sqrt{2}}(Y_{32} + Y_{3-2}), \quad (18e)$$

$$F_2(2) = \frac{\sqrt{3}}{4}(Y_{33} - Y_{3-3}) + \frac{\sqrt{5}}{4}(Y_{31} - Y_{3-1}), \quad (18f)$$

$$F_2(3) = -i\frac{\sqrt{3}}{4}(Y_{33} + Y_{3-3}) + i\frac{\sqrt{5}}{4}(Y_{31} + Y_{3-1}), \quad (18g)$$

and the corresponding coefficients can be obtained by

$$\epsilon_0 = \frac{4\pi}{3AR^3} \int d^3r \rho_v(\boldsymbol{r}) r^3 A_2, \quad (19a)$$

$$\epsilon_1(i) = \frac{4\pi}{3AR^3} \int d^3r \rho_v(\boldsymbol{r}) r^3 F_1(i), \quad (19b)$$

$$\epsilon_2(i) = \frac{4\pi}{3AR^3} \int d^3r \rho_v(\boldsymbol{r}) r^3 F_2(i). \quad (19c)$$

TABLE I. Pairing gaps (in MeV) calculated by the CDFT in 3D lattice space for ^{102,104}Zr, in comparison with the empirical values extracted from the three-point odd-even mass differences. The experimental masses are taken from AME2020 [61].

	^{102}Zr		^{104}Zr	
	Δ_n	Δ_p	Δ_n	Δ_p
Empirical	1.10	1.54	1.08	1.53
CDFT	1.12	1.55	1.00	1.49

For such a pure octupole shape, the intrinsic frame is defined by fixing $\epsilon_2 = 0$, and the range of the other four parameters should be restricted by the 48 transformations corresponding to the elements of the O_h group, to uniquely determine all possible octupole shapes without a repetition. As a result, one obtains that $\epsilon_0 \geqslant 0$ and $\epsilon_1(1) \geqslant \epsilon_1(2) \geqslant \epsilon_1(3) \geqslant 0$.

Hereafter, we denote the coefficients ϵ_0 and $\epsilon_1(1)$ by a_{32} and a_{30}, respectively, since they correspond to the tetrahedral and pear shapes, which satisfy the V_4 symmetry. The other two coefficients $\epsilon_1(2)$ and $\epsilon_1(3)$ are then denoted as a_{31} and a_{33} for consistency. Note that a nuclear shape with any two nonzero values of the three parameters a_{30}, a_{31}, and a_{33} would be beyond the V_4 symmetry.

III. NUMERICAL DETAILS

In this work, the point-coupling density functional PC-PK1 [57] is used. For the 3D lattice space, the step sizes and the grid numbers along the x, y, and z axes are chosen as 1 fm and 30, respectively. Similar to Ref. [43], the neutron and proton pairing strengths $G_n = -330$ MeV fm^3 and $G_p = -430$ MeV fm^3, are determined by reproducing the empirical pairing gaps of ^{102,104}Zr, which are obtained with the three-point odd-even mass differences formula [60] (see Table I).

IV. RESULTS AND DISCUSSION

We first discuss the efficiency of the PCG-F method in the self-consistent CDFT calculations for the ground state of ^{110}Zr. In Fig. 1, the maximum energy dispersion $[\langle h^2 \rangle - \langle h \rangle^2]_{max}$ for the occupied single-particle states and the maximum absolute difference ΔU between the mean potentials at two adjacent iterations are shown, in comparison with the results given by the IHM. For the PCG-F method, it takes only 84 iterations to achieve the convergence, i.e., $[\langle h^2 \rangle - \langle h \rangle^2]_{max} \leqslant 10^{-8}$ MeV^2 and $\Delta U \leqslant 10^{-2}$ MeV, while it requires more than 170 iterations for the IHM to reach the same accuracy. The difference between the total energies obtained in these two methods is smaller than 10^{-5} MeV. The total computational time for the PCG-F method is 386 min with the Intel(R) Xeon(R) CPU E5-2680, and it saves 52% of the computational time as compared with the IHM calculations. As seen in Ref. [56], compared with the IHM, the PCG-F method gives a much faster convergence in solving the Dirac equation with a given potential. The present results prove that the PCG-F method is more efficient than the IHM in the

TABLE II. The octupole deformation parameters a_{30}, a_{31}, a_{32}, and a_{33}, and the total energies E for the two lowest energy states of ^{110}Zr calculated by the CDFT in 3D lattice space.

a_{30}	a_{31}	a_{32}	a_{33}	E [MeV]
0.00	0.00	0.15	0.00	−902.49
0.15	0.11	0.00	0.11	−902.42

self-consistent CDFT calculations as well. This is not trivial because, during the self-consistent solution of the CDFT in 3D lattice space, the Dirac equation is not exactly solved until the self-consistency is achieved. In the following, we apply the framework of the PCG-F method to study the tetrahedral shape of ^{110}Zr.

Figure 2 depicts the one-dimensional potential energy curves of ^{110}Zr calculated with the CDFT in 3D lattice space by imposing different symmetry restrictions: (i) axial and reflection symmetry (AS & RS), (ii) axial symmetry and reflection asymmetry (AS & RA), (iii) V_4 symmetry, and (iv) full deformation space including all deformation degrees of freedom (Full). There are two energy minima in all cases, i.e., the ground state at $a_{20} \approx 0.00$ and a prolate minimum at $a_{20} \approx 0.50$. The ground-state energy varies visibly in the calculations with different symmetry restrictions. A spherical ground state is obtained if one assumes axial and reflection symmetry. The ground-state energy is lowered by about 0.4 MeV if one releases the restriction of reflection symmetry. It is lowered further by about 0.5 MeV if the nonaxial degrees of freedom are allowed under the V_4 symmetry. This ground state has a pure tetrahedral shape, and it is consistent with the results obtained in the previous MDC-CDFT calculations [43].

Thanks to the solutions in the 3D lattice space, one could remove all symmetry restrictions, and the results are shown by open circles in Fig. 2. Both the energy and the deformation of the ground state barely change. Such a pure octupole shape can be parametrized with the deformation parameters a_{30}, a_{31}, a_{32}, and a_{33} by defining a new intrinsic frame as mentioned in Sec. II.

In Table II, the calculated ground-state energy and octupole deformation parameters for the ground state of ^{110}Zr are listed. In addition to the ground state, a state whose energy is very close to the ground-state energy is also listed in Table II. The same results are found in the calculations with the same box size but a smaller step size of 0.8 fm. From Table II, one could see that although the ground-state energy and the deformation barely change, the pear-shaped isomeric state found in the previous work with V_4 symmetry [43] is significantly lowered in energy when the a_{31} and a_{33} degrees of freedom are allowed. The energy difference between the two state is only 0.07 MeV, indicating an interesting possible shape coexistence in ^{110}Zr.

We further investigate the effect of the deformations beyond V_4 symmetry on the two lowest energy states in ^{110}Zr. In Fig. 3, we show the potential energy surfaces in the (a_{30}, a_{32}) (a) and (a_{31}, a_{33}) [(b) and (c)] planes. In Fig. 3(a), the a_{31} and a_{33} deformations are always constrained to zero. It shows a well-developed tetrahedral ground state with $(a_{30}, a_{32}) \approx (0, 0.15)$ and a pear-like isomeric state at $(a_{30}, a_{32}) \approx (0.15, 0)$. The barrier between the two minima is about 0.5 MeV. This is consistent with the previous study with V_4 symmetry [43]. In the present work beyond V_4 symmetry, however, the effects of the a_{31} and a_{33} deformations can be analyzed.

As seen in Figs. 3(b) and 3(c), the deformations (a_{30}, a_{32}) are constrained to $(0, 0.15)$ and $(0.15, 0)$ in the (a_{31}, a_{33}) planes, respectively. Both energy surfaces are symmetric with respect to the diagonals since one can prove that the two intrinsic shapes corresponding to $a_{31} > a_{33}$ and $a_{31} < a_{33}$ are indeed identical by renaming the three axes of the intrinsic frame. In Fig. 3(b), the tetrahedral ground state with $a_{31} = a_{33} = 0$ remains, while the potential energy surface is soft in the direction from diagonal to abscissa. In contrast, as seen in Fig. 3(c), the pear-like isomeric state at $a_{31} = a_{33} = 0$ is no longer an energy minimum but a saddle point, and an even lower energy state with $a_{31} = a_{33} \approx 0.11$ appears. The shape with $a_{31} = a_{33} \approx 0.11$ is quite different from the tetrahedral shape of the ground state, but their energies differ by only 0.07 MeV. This again indicates an interesting possible shape coexistence in ^{110}Zr.
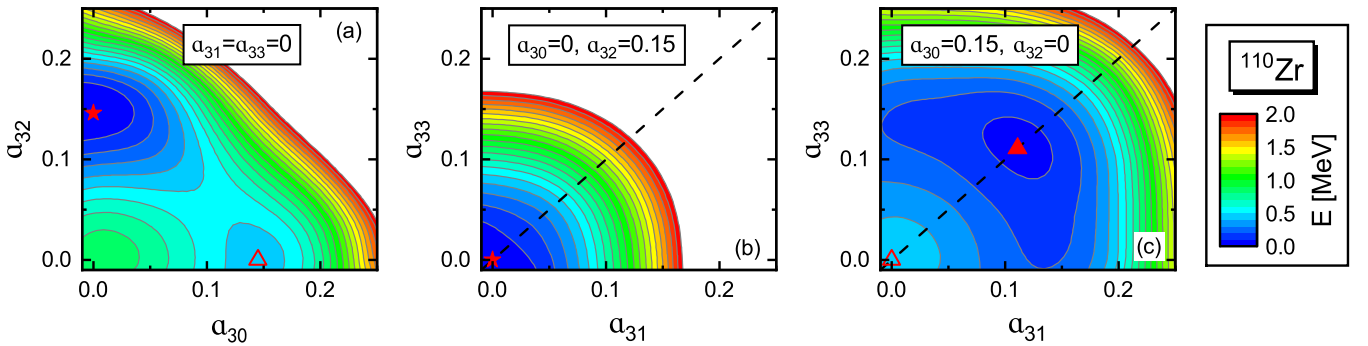

FIG. 3. The potential energy surfaces of ^{110}Zr in the (a_{30}, a_{32}) (a) and (a_{31}, a_{33}) [(b) and (c)] planes. The energies are normalized with respect to the ground-state energy, and the contour interval is 0.1 MeV. Note that a_{31} and a_{33} are always constrained to zero in (a), where the tetrahedral minimum and the pear-like minimum are indicated by a solid star and an open triangle, respectively. In (b), a_{30} and a_{32} are respectively constrained to 0 and 0.15, and the solid star corresponds to the tetrahedral minimum in (a). In (c), a_{30} and a_{32} are respectively constrained to 0.15 and 0, where the open triangle corresponds to the pear-like minimum in (a), and the solid one represents an even lower energy state. The dashed lines are diagonals in (b) and (c).
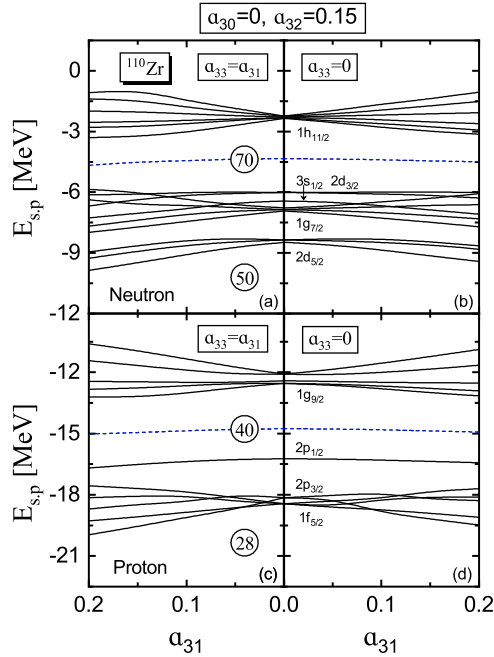
FIG. 4. Single-particle levels of ^{110}Zr as a function of a_{31} with $a_{30} = 0$ and $a_{32} = 0.15$. In (a) and (c), a_{33} is fixed to be identical to a_{31}, and for (b) and (d), a_{33} is fixed to zero. The levels are labeled by the corresponding spherical quantum number of their main component. The dashed lines represent the Fermi levels.

For a microscopic understanding, the single-particle levels of ^{110}Zr near the Fermi surface are shown in Figs. 4 and 5 as a function of a_{31} with, respectively, $a_{30} = 0$, $a_{32} = 0.15$ and $a_{30} = 0.15$, $a_{32} = 0$. In panels (a) and (c) of Figs. 4 and 5, we assume $a_{33} = a_{31}$, which means that the single-particle levels
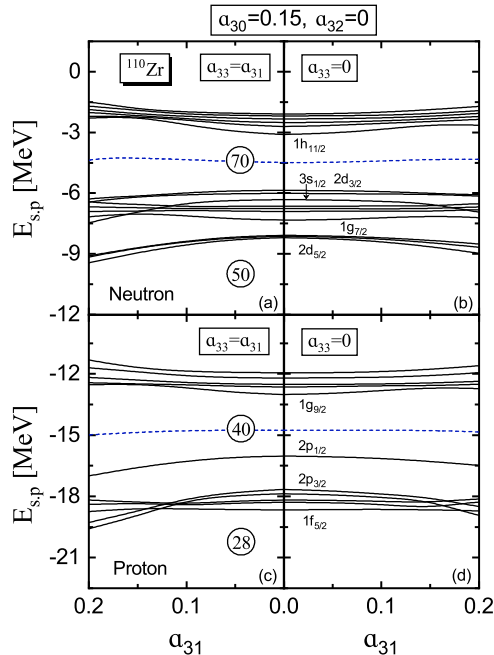

FIG. 5. Same as Fig. 4, but with $a_{30} = 0.15$ and $a_{32} = 0$.

are evolved along the diagonals as depicted in panels (b) and (c) of Fig. 3. Nevertheless, in panels (b) and (d) of Figs. 4 and 5, we assume $a_{33} = 0$, which means that the single-particle levels are evolved along the abscissas as depicted in panels (b) and (c) of Fig. 3.

In Fig. 4, at $a_{31} = 0$, the single-particle levels split into multiplets with degeneracies equal to the irreducible representations of the T_d^D group due to the nonzero a_{32} values. One can see dramatic energy gaps at $N = 70$ and $Z = 40$, and they are gradually narrowed with increasing a_{31}. As a result, an energy minimum at $a_{31} = a_{33} = 0$ should be expected, which just corresponds to the ground state of ^{110}Zr. Moreover, the soft nature of the potential energy surface from diagonal to abscissa in Fig. 3(b) should be associated with the nearly symmetric evolution behavior along a_{31} for the calculated single-particle levels with $a_{33} = a_{31}$ and $a_{33} = 0$.

In Fig. 5, the energy gaps at $N = 70$ and $Z = 40$ grow gradually with increasing a_{31}, so it explains the significant influence of the a_{31} and a_{33} deformations on the energy minimum as depicted in Fig. 3(c). In addition, the soft nature of the potential energy surface from diagonal to abscissa in Fig. 3(c) is also associated with the nearly symmetric evolution behavior along a_{31} for the calculated single-particle levels with $a_{33} = a_{31}$ and $a_{33} = 0$.

V. SUMMARY

In summary, the CDFT has been solved in 3D lattice space by implementing the PCG-F method. It considerably improves the computational efficiency compared to the previous inverse Hamiltonian method. Based on this framework, the shape of ^{110}Zr has been studied in the full deformation space. It is found that although the ground-state energy and deformation are consistent with the previous study [43], the pear-shaped isomeric state is significantly lowered in energy. The energy difference between the two states is only 0.07 MeV, indicating an interesting possible shape coexistence in ^{110}Zr. Moreover, the effect of the deformation degrees of freedom beyond V_4 symmetry is analyzed with the evolution of the single-particle levels near the Fermi surface. It is seen that the single-particle energy gaps at $N = 70$ and $Z = 40$ play a crucial role.

Similar effects may also exist in other nuclei. The present work has demonstrated the importance of full deformation space calculations for the tetrahedral states. Based on this new efficient method for the CDFT in 3D lattice space, works along this line are in progress.

[1] A. Bohr and B. R. Mottelson, *Nuclear Structure*, Vol. II (Benjamin, New York, 1975).

[2] S. Frauendorf and J. Meng, Nucl. Phys. A **617**, 131 (1997).

[3] S. W. Ødegård, G. B. Hagemann, D. R. Jensen, M. Bergström, B. Herskind, G. Sletten, S. Törmänen, J. N. Wilson, P. O. Tjøm, I. Hamamoto, K. Spohr, H. Hübel, A. Görgen, G. Schönwasser, A. Bracco, S. Leoni, A. Maj, C. M. Petrache, P. Bednarczyk, and D. Curien, Phys. Rev. Lett. **86**, 5866 (2001).

[4] K. Starosta, T. Koike, C. J. Chiara, D. B. Fossan, D. R. LaFosse, A. A. Hecht, C. W. Beausang, M. A. Caprio, J. R. Cooper, R. Krücken, J. R. Novak, N. V. Zamfir, K. E. Zyromski, D. J. Hartley, D. L. Balabanski, J.-Y. Zhang, S. Frauendorf, and V. I. Dimitrov, Phys. Rev. Lett. **86**, 971 (2001).

[5] J. Meng, J. Peng, S. Q. Zhang, and S.-G. Zhou, Phys. Rev. C **73**, 037303 (2006).

[6] P. A. Butler and W. Nazarewicz, Rev. Mod. Phys. **68**, 349 (1996).

[7] P. A. Butler, J. Phys. G: Nucl. Part. Phys. **43**, 073002 (2016).

[8] P. W. Zhao and Z. P. Li, Int. J. Mod. Phys. E **27**, 1830007 (2018).

[9] P. A. Butler, Proc. R. Soc. A. **476**, 20200202 (2020).

[10] S. Frauendorf, Rev. Mod. Phys. **73**, 463 (2001).

[11] Y. Y. Wang, X. H. Wu, S. Q. Zhang, and J. Meng, Sci. Bull. **65**, 2001 (2020).

[12] T. Inui, Y. Tanabe, and Y. Onodera, *Group Theory and Its Applications in Physics*, Vol. 78 (Springer-Verlag, Berlin, 1990).

[13] X. Li and J. Dudek, Phys. Rev. C **49**, R1250 (1994).

[14] J. Dudek, A. Góźdź, N. Schunck, and M. Miśkiewicz, Phys. Rev. Lett. **88**, 252502 (2002).

[15] J. Dudek, J. Dobaczewski, N. Dubray, A. Góźdź, V. Pangon, and N. Schunck, Int. J. Mod. Phys. E **16**, 516 (2007).

[16] W. D. Heiss, R. A. Lynch, and R. G. Nazmitdinov, Phys. Rev. C **60**, 034303 (1999).

[17] K.-I. Arita and Y. Mukumoto, Phys. Rev. C **89**, 054308 (2014).

[18] J. Dudek, A. Góźdź, and N. Schunck, Acta. Phys. Pol. B **34**, 2491 (2003).

[19] R. A. Bark, J. F. Sharpey-Schafer, S. M. Maliage, T. E. Madiba, F. S. Komati, E. A. Lawrie, J. J. Lawrie, R. Lindsay, P. Maine, S. M. Mullins, S. H. T. Murray, N. J. Ncapayi, T. M. Ramashidza, F. D. Smit, and P. Vymers, Phys. Rev. Lett. **104**, 022501 (2010).

[20] M. Jentschel, W. Urban, J. Krempel, D. Tonev, J. Dudek, D. Curien, B. Lauss, G. de Angelis, and P. Petkov, Phys. Rev. Lett. **104**, 222502 (2010).

[21] J. Dudek, D. Curien, N. Dubray, J. Dobaczewski, V. Pangon, P. Olbratowski, and N. Schunck, Phys. Rev. Lett. **97**, 072501 (2006).

[22] Q. T. Doan, A. Vancraeyenest, O. Stézowski, D. Guinet, D. Curien, J. Dudek, P. Lautesse, G. Lehaut, N. Redon, C. Schmitt, G. Duchêne, B. Gall, H. Molique, J. Piot, P. T. Greenlees, U. Jakobsson, R. Julin, S. Juutinen, P. Jones, S. Ketelhut, M. Nyman, P. Peura, P. Rahkila, A. Góźdź, K. Mazurek, N. Schunck, K. Zuber, P. Bednarczyk, A. Maj, A. Astier, I. Deloncle, D. Verney, G. de Angelis, and J. Gerl, Phys. Rev. C **82**, 067306 (2010).

[23] B. Ackermann, H. Baltzer, C. Ensel, K. Freitag, V. Grafen, C. Günther, P. Herzog, J. Manns, M. Marten-Tölle, U. Müller, J. Prinz, I. Romanski, R. Tölle, J. deBoer, N. Gollwitzer, and H. Maier, Nucl. Phys. A **559**, 61 (1993).

[24] S. S. Ntshangase, R. A. Bark, D. G. Aschman, S. Bvumbi, P. Datta, P. M. Davidson, T. S. Dinoko, M. E. A. Elbasher, K. Juhász, E. M. A. Khaleel, A. Krasznahorkay, E. A. Lawrie, J. J. Lawrie, R. M. Lieder, S. N. T. Majola, P. L. Masiteng, H. Mohammed, S. M. Mullins, P. Nieminen, B. M. Nyakó, P. Papka, D. G. Roux, J. F. Sharpey-Shafer, O. Shirinda, M. A. Stankiewicz, J. Timár, and A. N. Wilson, Phys. Rev. C **82**, 041305(R) (2010).

[25] T. Sumikama, K. Yoshinaga, H. Watanabe, S. Nishimura, Y. Miyashita, K. Yamaguchi, K. Sugimoto, J. Chiba, Z. Li, H. Baba, J. S. Berryman, N. Blasi, A. Bracco, F. Camera, P. Doornenbal, S. Go, T. Hashimoto, S. Hayakawa, C. Hinke, E. Ideguchi, T. Isobe, Y. Ito, D. G. Jenkins, Y. Kawada, N. Kobayashi, Y. Kondo, R. Krücken, S. Kubono, G. Lorusso, T. Nakano, M. Kurata-Nishimura, A. Odahara, H. J. Ong, S. Ota, Z. Podolyák, H. Sakurai, H. Scheit, K. Steiger, D. Steppenbeck, S. Takano, A. Takashima, K. Tajiri, T. Teranishi, Y. Wakabayashi, P. M. Walker, O. Wieland, and H. Yamaguchi, Phys. Rev. Lett. **106**, 202501 (2011).

[26] A. Dobrowolski, A. Góźdź, K. Mazurek, and J. Dudek, Int. J. Mod. Phys. E **20**, 500 (2011).

[27] D. J. Hartley, L. L. Riedinger, R. V. F. Janssens, S. N. T. Majola, M. A. Riley, J. M. Allmond, C. W. Beausang, M. P. Carpenter, C. J. Chiara, N. Cooper, D. Curien, B. J. P. Gall, P. E. Garrett, F. G. Kondev, W. D. Kulp, T. Lauritsen, E. A. McCutchan, D. Miller, S. Miller, J. Piot, N. Redon, J. F. Sharpey-Schafer, J. Simpson, I. Stefanescu, X. Wang, V. Werner, J. L. Wood, C.-H. Yu, S. Zhu, and J. Dudek, Phys. Rev. C **95**, 014321 (2017).

[28] N. Schunck, J. Dudek, A. Góźdź, and P. H. Regan, Phys. Rev. C **69**, 061305(R) (2004).

[29] J. Dudek, D. Curien, D. Rouvel, K. Mazurek, Y. R. Shimizu, and S. Tagami, Phys. Scr. **89**, 054007 (2014).

[30] P. Jachimowicz, M. Kowal, and J. Skalski, Phys. Rev. C **95**, 034329 (2017).

[31] J. Dudek, D. Curien, I. Dedes, K. Mazurek, S. Tagami, Y. R. Shimizu, and T. Bhattacharjee, Phys. Rev. C **97**, 021302(R) (2018).

[32] R. Bijker and F. Iachello, Phys. Rev. Lett. **112**, 152501 (2014).

[33] Z. C. Gao, Y. S. Chen, and J. Meng, Chin. Phys. Lett. **21**, 806 (2004).

[34] Y. S. Chen and Z. C. Gao, Nucl. Phys. A **834**, 378c (2010).

[35] S. Takami, K. Yabana, and M. Matsuo, Phys. Lett. B **431**, 242 (1998).

[36] M. Yamagami, K. Matsuyanagi, and M. Matsuo, Nucl. Phys. A **693**, 579 (2001).

[37] P. Olbratowski, J. Dobaczewski, P. Powałowski, M. Sadziak, and K. Zberecki, Int. J. Mod. Phys. E **15**, 333 (2006).

[38] K. Zberecki, P. Magierski, P.-H. Heenen, and N. Schunck, Phys. Rev. C **74**, 051302(R) (2006).

[39] K. Zberecki, P.-H. Heenen, and P. Magierski, Phys. Rev. C **79**, 014319 (2009).

[40] S. Tagami, Y. R. Shimizu, and J. Dudek, Phys. Rev. C **87**, 054306 (2013).

[41] S. Tagami, Y. R. Shimizu, and J. Dudek, J. Phys. G: Nucl. Part. Phys. **42**, 015106 (2015).

[42] S. Miyahara and H. Nakada, Phys. Rev. C **98**, 064318 (2018).

[43] J. Zhao, B.-N. Lu, E.-G. Zhao, and S.-G. Zhou, Phys. Rev. C **95**, 014320 (2017).

[44] K. Wang and B.-N. Lu, Commun. Theor. Phys. **74**, 015303 (2022).

[45] *Relativistic Density Functional for Nuclear Structure*, International Review of Nuclear Physics, Vol. 10, edited by J. Meng (World Scientific, Singapore, 2016).

[46] P. Ring, Prog. Part. Nucl. Phys. **37**, 193 (1996).

[47] D. Vretenar, A. V. Afanasjev, G. A. Lalazissis, and P. Ring, Phys. Rep. **409**, 101 (2005).

[48] J. Meng, H. Toki, S. G. Zhou, S. Q. Zhang, W. H. Long, and L. S. Geng, Prog. Part. Nucl. Phys. **57**, 470 (2006).

[49] J. Meng, J. Peng, S. Q. Zhang, and P. W. Zhao, Front. Phys. **8**, 55 (2013).

[50] Z. X. Ren and P. W. Zhao, Phys. Rev. C **102**, 021301(R) (2020).

[51] Y. Zhang, H. Z. Liang, and J. Meng, Int. J. Mod. Phys. E **19**, 55 (2010).

[52] Y. Tanimura, K. Hagino, and H. Z. Liang, Prog. Theor. Exp. Phys. **2015**, 073D01 (2015).

[53] Z. X. Ren, S. Q. Zhang, P. W. Zhao, N. Itagaki, J. A. Maruhn, and J. Meng, Sci. China Phys. Mech. Astron. **62**, 112062 (2019).

[54] K. Hagino and Y. Tanimura, Phys. Rev. C **82**, 057301 (2010).

[55] Z. X. Ren, S. Q. Zhang, and J. Meng, Phys. Rev. C **95**, 024313 (2017).

[56] B. Li, Z. X. Ren, and P. W. Zhao, Phys. Rev. C **102**, 044307 (2020).

[57] P. W. Zhao, Z. P. Li, J. M. Yao, and J. Meng, Phys. Rev. C **82**, 054319 (2010).

[58] W. Ryssens, V. Hellemans, M. Bender, and P.-H. Heenen, Comput. Phys. Commun. **190**, 231 (2015).

[59] I. Hamamoto, Xi zhen Zhang, and Hong-xing Xie, Phys. Lett. B **257**, 1 (1991).

[60] M. Bender, K. Rutz, P.-G. Reinhard, and J. A. Maruhn, Eur. Phys. J. A **8**, 59 (2000).

[61] M. Wang, W. J. Huang, F. G. Kondev, G. Audi, and S. Naimi, Chin. Phys. C **45**, 030003 (2021).